JGR Space Physics

RESEARCH ARTICLE

10.1029/2018JA026124

Key Points:

- A 3-D model fit to 2-D images can extract magnetopause and bow shock boundaries even when the model is not an exact fit to the observations
- Orbital bias produced model/observation differences is within the science goal of the SMILE mission for large part of the orbit
- When using the simplex method, the initial guess must be chosen carefully to avoid false minima

Correspondence to:
A. M. Jorgensen and T. Sun,
anders.m.jorgensen@nmt.edu;
trsun@spaceweather.ac.cn

Citation:
Jorgensen, A. M., Sun, T., Wang, C., Dai, L., Sembay, S., Zheng, J. H., & Yu, X. Z. (2019). Boundary Detection in Three Dimensions With Application to the SMILE Mission: The Effect of Model-Fitting Noise. *Journal of Geophysical Research: Space Physics*, *124*, 4341–4355. https://doi.org/10.1029/2018JA026124

Received 21 SEP 2018
Accepted 15 APR 2019
Accepted article online 1 MAY 2019
Published online 24 JUN 2019

Boundary Detection in Three Dimensions With Application to the SMILE Mission: The Effect of Model-Fitting Noise

Anders M. Jorgensen[1], Tianran Sun[2], Chi Wang[2], Lei Dai[2], Steve Sembay[3], Jianhua Zheng[4], and Xizheng Yu[4]

[1]Electrical Engineering Department, New Mexico Institute of Mining and Technology, Socorro, NM, USA, [2]State Key Laboratory of Space Weather, National Space Science Center, Chinese Academy of Sciences, Beijing, China, [3]Department of Physics and Astronomy, University of Leicester, Leicester, UK, [4]Laboratory of System Simulation and Concurrent Design Technology, National Space Science Center, Chinese Academy of Sciences, Beijing, China

Abstract The magnetosheath and near-Earth solar wind emit X-rays due to charge-exchange between the extended atmosphere and highly ionized particles in the solar wind. These emissions can be used to remotely sense the dynamic processes in this region. The Solar Wind Magnetosphere Ionosphere Link Explorer mission will carry out these measurements. In a previous paper, we looked at the effect of photon counting statistics on determining the location of the magnetopause and bow shock. In this paper we explore, through simulations, the more challenging question of orbital viewing geometry bias when the model and the emissions do not match each other exactly. Our simulations conclude that while care must be taken to avoid false minima in the fitting, there is very little to no orbital bias in extracting the position and large-scale shape of the magnetopause and bow shocks from 2-D X-ray images from the future Solar Wind Magnetosphere Ionosphere Link Explorer mission.

1. Introduction

X-ray imaging of the solar wind charge exchange (SWCX) processes in Earth's magnetosheath and nearby solar wind can provide a wealth of information about the dynamic processes which take place in those regions. Sibeck et al. (2018) provide a very thorough and extensive review of developments in the field of X-ray imaging and related fields. SWCX was originally proposed by Cravens (1997) as an explanation for X-ray emissions from comet Hyakutake reported by Lisse et al. (1996). Since then, astronomical missions have confirmed SWCX in the magnetosheath (Carter et al., 2010; Snowden et al., 2009). Because these processes often operate on minute time scales, it is important to be able to snapshot image on a similar time scale to minimize smearing of the structures being observed. The Solar Wind Magnetosphere-Ionosphere Link Explorer (SMILE; Raab et al., 2016) mission will carry out these measurements. SMILE will image the subsolar region of the magnetosphere, magnetosheath, and bow shock from an elliptical orbit with an altitude above the north pole of approximately 19 Earth radii. The 2-D images present the challenge of extracting the 3-D X-ray emissions structures from these images. Extracting the large-scale structures of this region from the images can be done by fitting a parameterized model to the images. We have previously developed such a model and used it to determine the necessary count rates required to determine locations of boundaries to specified accuracies and found that the required count rates correspond well with the expected count rates from the SMILE mission (Jorgensen et al., 2019).

This paper extends the analysis in the paper by Jorgensen et al. (2019). In that paper we analyzed the effect of photon noise on the extraction of boundary parameters in 2-D images of optically thin targets, with focus particularly on X-ray imaging of the Earth's magnetopause, magnetosheath, and bow shock, with the future Chinese-European SMILE mission.

The introduction to that paper includes a detailed discussion of the background to this topic, and for that reason, we will limit ourselves here to discussing some key points as well as the results of that paper. Jorgensen et al. (2019) examined the effect of Poisson noise in reconstructing the magnetopause and bow shock from different viewing geometries and different background and foreground count levels. In that work we found that there is no detectable bias due to viewing geometry as a result of finite count rates although the uncertainty is affected by viewing geometry. The effect of viewing geometry on uncertainty is a result of the amount of the boundary which is visible in the image. For example, if a larger section of the magnetopause is visible in an image, the uncertainty in reconstructing the magnetopause is smaller, for a given foreground and background count-rate.

For the case of the SMILE mission, we also examined two different solar wind conditions for a representative apogee viewing geometry, one with high particle flux ($n_{sw}v_{sw}$) and one with low particle flux. The high solar wind flux case was $n_{sw} = 25$ cm^{-3} and $v_{sw} = 600$ km/s, and the low solar wind flux case was $n_{sw} = 5$ cm^{-3} and $v_{sw} = 400$ km/s. For the high solar wind flux case, we found that after 1 min of integration, there would be 0.6 foreground counts per pixel and 0.3 background counts per pixel. The simulations then revealed that the contribution of the photon counting statistics to the uncertainty would amount to an uncertainty of 0.04 R_E on the position of the subsolar point of the magnetopause, r_0^{mp}, and an uncertainty of 0.03 R_E on the position of the subsolar point on the bow shock, r_0^{bs}.

For the low solar wind flux case, we found that after 20 min of integration, there would be 0.8 foreground counts per pixel on average and 5 background counts per pixel. In this scenario the simulations revealed that the contribution of photon counting statistics to the uncertainty is 0.08 R_E on the location of the subsolar point on the magnetopause, r_0^{mp}, and 0.1 R_E on the location of the subsolar point of the bow shock, r_0^{bs}.

Part of the SMILE science goal is determining the boundary positions to an accuracy of ~0.1 R_E. Thus, we concluded in that paper that from the point of view of photon counting statistics, the SMILE Soft X-ray Imager (SXI) design will meet the SMILE mission science goal on short time scales (1 min) for higher solar wind fluxes and somewhat longer time scales (e.g., 20 min) for lower solar wind fluxes.

There are other sources of noise and error in the measurement than Poisson noise. In the present paper, we explore the effect of model noise and also briefly the effect of fitting algorithm noise. Model noise is the mismatch between the model and the observations that the model is intended to fit. If the model does not exactly reproduce the observations, then fitting the model to the observations introduces an error or bias or noise as a result. This is what we refer to as the model noise. Fitting algorithm noise is the name we use for the effect of the fitting algorithm returning a local minimum instead of the global minimum. This effect is a function of the algorithm chosen. We are currently using a simple gradient-based algorithm which does not automatically find the global minimum.

To summarize the findings of the present paper, we find that the model we have chosen is a sufficiently good fit to the simulated observations from a magnetohydrodynamics (MHD) model and that there is only minimal bias introduced. We also find that the model is sufficiently complex and the cost-function landscape is sufficiently complex that a simple hill-climbing algorithm will not find the global optimum except when the initial guess is very carefully selected. Tests show that our choice of initial conditions does appear to find the global minimum or at least a minimum which is close enough to the global minimum that we cannot distinguish it.

2. Methodology

In this paper we intend to answer two questions. The first question is whether the vantage point viewing geometry affects the values of parameters extracted from model fits to images. We are specifically interested in the view from the SMILE SXI camera looking at X-ray emissions from the vicinity of the nose of the magnetopause. However, the answers may well inform broader questions. The second question is whether and to what extent a simple hill-climbing algorithm is sufficient for finding the global optimal fit. Again, this is done specifically for the model we are using to represent the X-ray emissions in the vicinity of the nose of the magnetopause, but it may inform a broader range of problems.

In the first case, to determine how close the parameters are to truth, we must first decide what is truth. Because the analytical model is not a perfect fit to the simulated observation from the MHD model, we will obtain different parameters depending on how we carry out the fit, including what cost function we use and what set or subset of data points we fit to. We must also avoid false minima (non-global minima) in the cost function, so we must start the fit close to the truth value.

In the second case, to determine how complicated the cost-function landscape is and how determined fits compare with the global optimal fit, we must have a good idea of what the global optimal fit is.

For these reasons, we first spend a large part of the paper arriving at the best global fit of the model to the 3-D simulated emissions from the MHD model, without involving fitting to the images. The details of how we do this will be described in section 3 as we proceed through the steps. Second, using the best global fit as an initial guess, we fit the model to the 2-D images simulated from the MHD simulations and compare the fitted parameters as well as the depth of minima to the best global fit of the model to the 3-D simulated emissions. Third and finally, we examine the cost-function landscape for false minima by redoing the fit of the model to the 2-D images with randomly distributed initial guesses around the previously determined best fit to the 2-D images and compare the parameters and the depth of the minima.

In the following, refer to the magnetopause and bow shock boundaries. We use the flux method to locate the magnetopause position in the MHD result. The flux drops sharply at the boundary, and the magnetopause can be defined as the radius at which it has dropped to half of the solar wind level. This produces a smooth boundary specified on a grid.

2.1. Models

The models we fit to the X-ray emissions are the same models which were developed by Jorgensen et al. (2019), and the reader is asked to refer to that paper for more details. The models consists of a boundary model used for the magnetopause and the bow shock and a brightness model used for the regions between the boundaries. The boundary model is a generalization of the model by Shue et al. (1997) and has the following form

$$r(\theta,\phi) = \frac{r_y(\theta)\, r_z(\theta)}{\sqrt{\left[r_z(\theta)\cos\phi\right]^2 + \left[r_y(\theta)\sin\phi\right]^2}}, \tag{1}$$

where in accordance with Shue et al. (1997),

$$r_y(\theta) = r_0\left(\frac{2}{1+\cos\theta}\right)^{\alpha_y}, \tag{2}$$

and

$$r_z(\theta) = r_0\left(\frac{2}{1+\cos\theta}\right)^{\alpha_z}, \tag{3}$$

and where θ is the angle to the X axis and ϕ is the azimuthal angle in a right-hand sense around the X axis starting from the Y axis.

It is noted that for a simple magnetopause model given by equation (1), the cusp boundaries are neglected in the current study. And the X-ray emissions from the cusps, which are expected to be intensive (Sun et al., 2019), are also removed. Cusp emissions in real data can be blanked out if the magnetopause and cusps do not overlap. Therefore, the present approach can be usable on real data. Nevertheless, the cusps are very important regions. We are now working on developing a method to derive the cusp boundary positions from the X-ray images.

The emissions model consists of three regions separated by two boundaries. The two boundaries are the magnetopause and the bow shock, both represented by equation (1) with different parameters r_0, α_y, and α_z for each. The three regions are the solar wind, located sunward ($+X$) of the bow shock boundary; the magnetosheath, located between the bow shock and the magnetopause boundaries; and the magnetosphere, located inside the magnetopause boundary. The mathematical form of the model is as follows:

$$F(\vec{r}) = \begin{cases} 0 & \text{inside MP} \\ \left(A_1 + B\sin^8\theta\right)\left(\frac{r}{r_{\mathrm{ref}}}\right)^{-(\alpha+\beta\sin^2\theta)} & \text{between MP and BS} \\ A_2\left(\frac{r}{r_{\mathrm{ref}}}\right)^{-3} & \text{outside BS} \end{cases}. \tag{4}$$

2.2. Fitting Approach

Images are computed in the same way that Jorgensen et al. (2019) did it. The value in each image pixel is the line integral through a model volume, using the approach described by Kronrod (1965). Simulated images were computed based on the MHD model X-ray emissions, whereas the images used in the fit were computed from the analytical model based on equation (4) for the emissions and equation (1) for each of the magnetopause and bow shock.

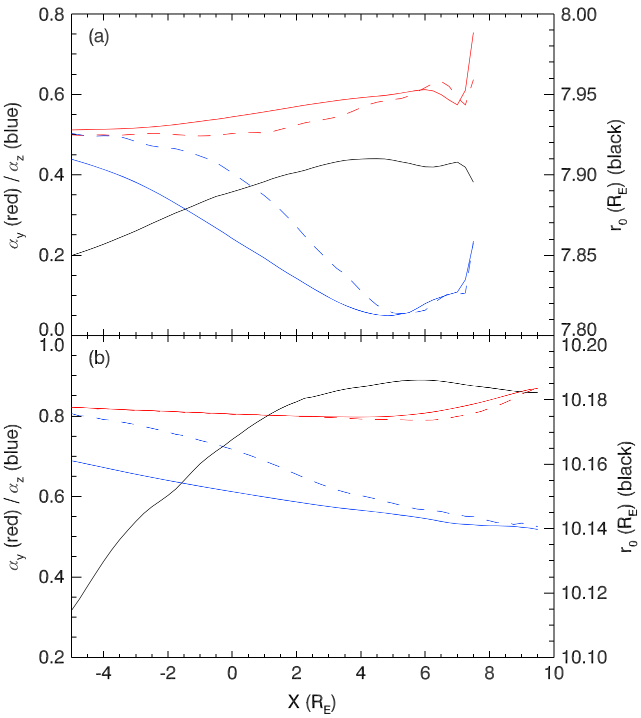

Figure 1. Fit of the boundary model, equation (1), to the magnetopause (a) and bow shock (b). The horizontal axis is GSM X. The solid curves are r_0 (black), α_y (red), and α_z (blue) best fit to the boundary sunward of X. The dashed curves are α_y (red) and α_z (blue) fit to points within 0.25 R_E of X while keeping $r_0 = 7.9\ R_E$ for the magnetopause and $r_0 = 10.18\ R_E$ for the bow shock.

The cost function is the mean-absolute deviation

$$e = \frac{1}{N}\sum_{i=1}^{N} |f_{i,\text{model}} - f_{i,\text{data}}|, \tag{5}$$

because it typically produces better results (in the sense that it looks like a better fit to the eye) than the least-squares fit when the model and data are not exact matches.

For finding the cost-function minimum, we use the simplex approach by Nelder and Mead (1965). Because it is not a global minimization algorithm, we carefully pick the starting point for the minimizer to be the fit to the 3-D distribution. It is too early to optimize the cost-function minimizer at this point (e.g., Wolpert & Macready, 1997).

3. Results

Here are the results of the simulations. We begin in section 3.1 with summarizing the work, which is then described in the following sections.

3.1. Summary of the Approach

We begin with the same data set used by Jorgensen et al. (2019) in which the grid of radial distance to the magnetopause and bow shock boundaries is computed as a function of θ and ϕ, and the 3-D X-ray emission rate is computed from the 3-D MHD plasma density, velocity, and temperature.

The next step is to obtain the best fit boundary model to the 3-D distribution of X-ray emission for later comparison with the fits of the model to the 2-D images. The first step is to fit the boundary model directly to the grid of boundary points to get an initial good guess. We start that fit at the nominal boundary parameter values obtained by Jorgensen et al. (2019). Then we repeat that fit as a function of orbital position while including just the points in the grid which fall within the field-of-view (FOV) of the SXI camera, using the previous fit as initial guess. This will give us an idea of how the boundary fit changes with viewing geometry. Next, for each position in the orbit, we fit for the emission while holding the boundaries fixed at the value found in the previous fit and fitting to the 3-D emission points within the FOV of SXI. As initial guess, we use the emissions parameters obtained by Jorgensen et al. (2019). The final step in fitting the 3-D distribution is as follows. Using the best fit boundary parameters and emissions parameters at each orbital position as initial guess, we fit again to the 3-D emissions points within the FOV of SXI but, this time, fitting both the boundary parameters and the emission parameters, 11 parameters in total. These will be considered the best fit parameters to the 3-D emission distribution as a function of orbital position. The final step is to fit the model, including the boundaries parameters and the emissions parameters, to the 2-D images obtained at each point in the orbit. We use the best fit parameters from the 3-D distribution as the initial guess in order to minimize the likelihood of false minima. The fitted parameters from the 2-D images are compared with the best fit parameters from the 3-D emissions distribution fits, which will allow us to determine the errors and/or biases associated with fitting to the 2-D images.

In the following sections, we go into details of each step of the procedure just outlined in this subsection.

3.2. Fitting the Boundaries

The first step in the fitting is to estimate the best fit of the boundary model to the gridded boundary points. It is clear that the boundary models, equations (1) to (3), are not an exact fit to the magnetopause and bow shock models. This can be seen in Figure 4 (especially panels c and d) of Jorgensen et al. (2019) in which the model is overplotted on the measured boundary positions. Because the boundary model does not exactly match the gridded boundary points from the MHD model, the fitted parameters will depend on which points are included in the fit. It also depends on the cost function to be minimized, but we have already argued for using the mean-absolute difference as the cost function in section 2.2. Initially, for different values of geocentric solar magnetospheric (GSM) X, we fit the model to boundary points which are located sunward of X. The result is the solid curves in Figure 1. Figure 1a shows fits to the magnetopause, whereas Figure 1b

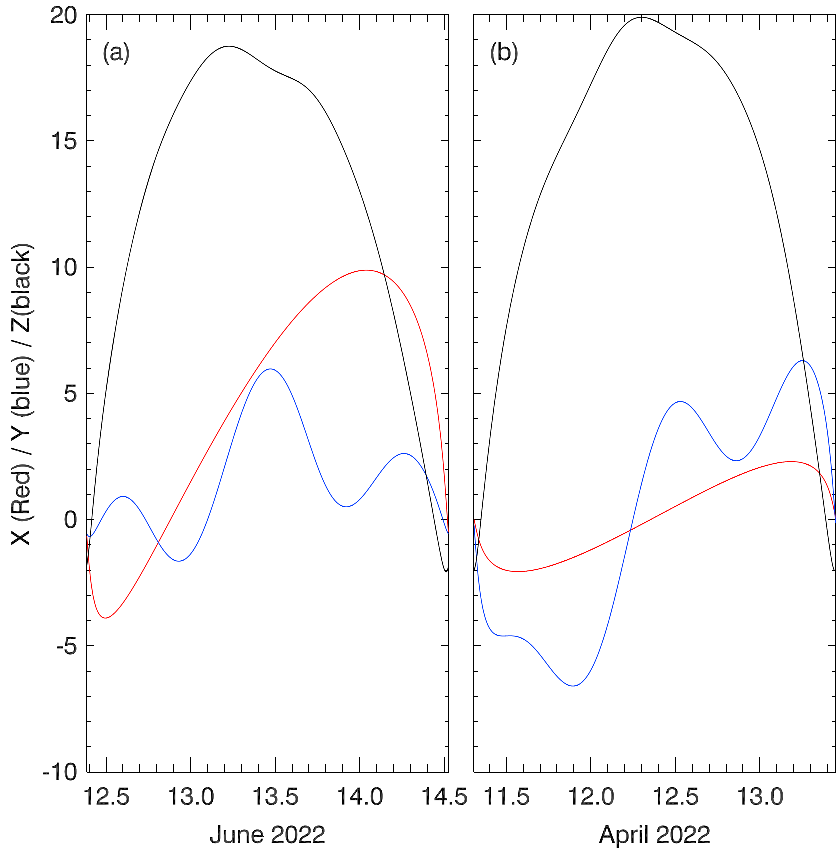

Figure 2. Location of the Solar Wind Magnetosphere Ionosphere Link Explorer spacecraft in two representative orbits taken from a Solar Wind Magnetosphere Ionosphere Link Explorer mission-planning simulation. We selected the June 2022 orbit to maximize the movement in the X direction, and we selected the April 2022 orbit to minimize the movement in the X direction.

shows fits to the bow shock. In each panel, the black curve is the value of r_0 referenced to the right-side axis, and the red curve α_y and the blue curve α_z both referenced to the left-side axis. The first thing to note is that the variation of the values of r_0 for the magnetopause and bow shock as a function of X is small, in fact smaller than the grid spacing in the MHD simulation (about 0.1 R_E). The next thing we note is that for both the magnetopause and the bow shock, the value of α_y is nearly independent of X. This happens when the model is a good fit to the data in the XY-plane. This is in fact what we observe in Figure 4 in Jorgensen et al. (2019). The values of α_y and α_z spike at X-values close to the magnetopause, but we can ignore that behavior for two reasons: When θ is small, the position of the boundary is only weakly dependent on the value of α; the algorithm which is used to determine the position of the magnetopause creates a small dent at the subsolar point due to the stagnation of magnetosheath flow at that point, and this artifact may be what the algorithm fits in that very small region.

To investigate the shape of the boundaries further, we fit for α_y and α_z for points located close to X (within a 0.25 R_E band centered at X). With this arrangement, having only a ring of points, we cannot constrain r_0, so we choose a nominal value which corresponds to the value obtained when fitting points near the subsolar point only, $r_0^{mp} = 7.90\ R_E$ and $r_0^{bs} = 10.18\ R_E$. The result is the dashed curves in Figure 1, where the colors have the same meaning as before, α_y in red and α_z in blue. The fact that the red dashed and solid curves are nearly identical is further confirmation that the model fits the boundaries well in the XY plane. That the red and blue dashed curves are nearly identical at about $X = -5\ R_E$ shows that the cross section of the magnetopause and bow shock is nearly circular at that point. To further improve the model of the boundaries, we can introduce parameterized functions for the dashed curves, particularly the curve for α_z for the magnetopause. We will not do this kind of parameterization in this paper but simply note that it may be useful in the future, especially if the variation can be expressed in a systematic way across different solar wind conditions. It is difficult to say how much of an improvement can be expected from a model

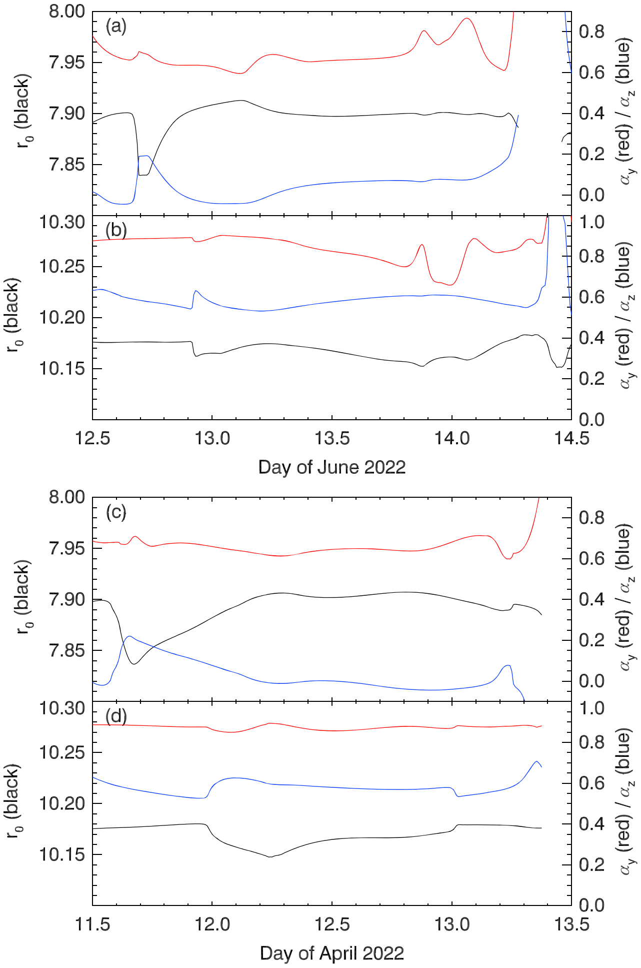

Figure 3. Fit of the boundary parameters to sections of the boundaries which fall within the field-of-view of the Solar Wind Magnetosphere Ionosphere Link Explorer SXI camera, as a function of position in the orbit. The times refer to the times in Figure 2. (a) and (b) are for the June 2022 orbit; (c) and (d) are for the April 2022 orbit. In each plot, (a) and (c) are for the magnetopause, and (b) and (d) are for the bow shock. In each panel, the black curve is the value of r_0, referenced to the axis on the left; the red curve is α_y and blue α_z, both referenced to the axis on the right.

except to say that the Poisson statistics of Jorgensen et al. (2019) is the limit. Another option is to use more sophisticated models. The sophisticated model by Lin et al. (2010) is an example of such. However, there are a number of practical problems of fitting such a complicated model. It is not obvious that it will improve the overall results. Even if the magnetopause model is good, it would need to be combined with a good magnetosheath model as well. In any case, more simulations can help in understanding how sophisticated models are required to be and that is in fact in our future plans in preparation for the SMILE mission launch.

3.3. Satellite Orbits

The remaining steps in the paper involve simulations and fits for different viewing geometries corresponding to different positions in an orbit. For this, we selected two representative simulated orbits for the SMILE mission from a orbit simulation produced as part of the SMILE mission planning. The two orbits are shown in GSM coordinates in Figure 2 as we expect that among the common space physics coordinate systems, this one will organize the data the best. We use the dates of the two simulations (June 2022 in Figure 2a and April 2022 in Figure 2b) from the original simulation as reference, but these should not be taken literally as an expectation that the spacecraft will actually be in those orbits on those dates. The June 2022 orbit was selected because it had a large range of X-coordinates, whereas the April 2022 orbit was selected for having X-coordinates which are close to zero. We selected these two orbits because we believe that they represent two extremes of viewing geometry, one which is more symmetric and less likely to see orbital bias (April 2022) and one which is less symmetric and more likely to exhibit orbital bias (June 2022).

3.4. Fitting the Boundaries as a Function of Orbital Viewing Geometries

The next step in the analysis is to fit boundary models to just the portion of the gridded boundary distances which are in the FOV of the SXI camera at different points in its orbit. This will allow us to compare the orbital viewing geometry effect of fitting the boundary directly with any orbital viewing geometry effect from fitting the 2-D images. As the initial guess for the parameters of the fit, we use some representative average values from the fit in Figure 1, $r_0^{mp} = 8$, $\alpha_y^{mp} = 0.5$, and $\alpha_z^{mp} = 0.5$ for the magnetopause and $r_0^{bs} = 10$, $\alpha_y^{bs} = 0.8$, and $\alpha_z^{bs} = 0.8$ for the bow shock. The viewing geometry is chosen to make the camera look at the GSM coordinate $(X, Y, Z) = (9.5, 0, 0)$ R_E at all times through a yaw rotation followed by a pitch rotation from a camera initially pointed in the GSM positive X direction with no roll (we are adopting standard flying terminology for the rotation angle with the camera pointing level along the axis of an aircraft body).

The results of the fits are shown in Figure 3. Figures 3a and 3b are for the June 2022 orbit, while Figures 3c and 3d are for the April 2022 orbit. Figures 3a and 3c are for the magnetopause, while Figures 3b and 3d are for the bow shock. In each panel, the black curve is r_0 referenced to the left-side axis, while the red and blue curves are α_y and α_z, respectively, referenced to the right-side axis. For the most part, the location of the subsolar point on the boundary remains almost independent of orbital position. There is a deviation of about 0.05 R_E for the magnetopause at the start of both orbits (Figure 3a, 12.6 to 12.8, and Figure 3c, 11.6 to 12.0) which are smaller than the grid size in the MHD simulation and also well within the science goal for the SMILE missions. The deviations in r_0 appear to be mirrored by deviations in α_z. This effect can be explained by the less good fit of the model in the XZ plane. Thus, different portions of the boundary may be best fit by different sets of parameters. Near the ends of the orbits, there is also large deviation of the fitted

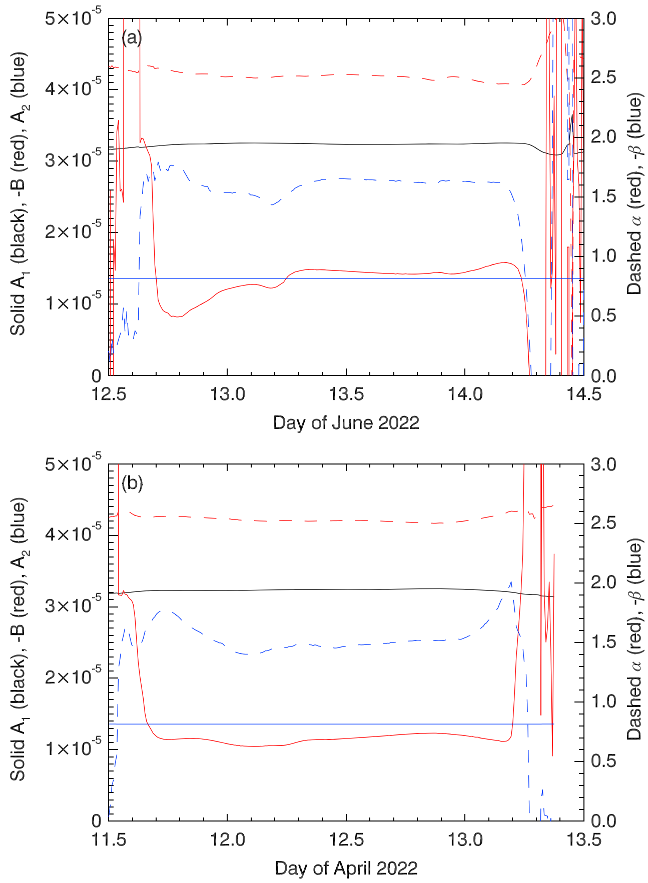

Figure 4. Fit of the emissions function parameters A_1, B, α, β, and A_2 as a function of position in the orbit for the two orbits while using for the boundaries the parameters previously fit in Figure 3. (a) is for the June 2022 orbit, and (b) is for the April 2022 orbit. In each panel, the parameters in equation (4) are plotted. The solid black curve is A_1, the solid red curve is $-B$, and the solid blue curve is A_2, all referenced to the left-side axis; the dashed red curve is α, and the dashed blue curve is $-\beta$, both referenced to the right-side axis.

parameters. This is also not surprising as the FOV of SXI will contain only relatively small portion of the boundary at the ends of the orbits.

3.5. Fitting the 3-D Emissions Function as a Function of Orbital Viewing Geometry

The next step is to fit for the emissions parameters as a function of orbital viewing geometry. We do this fit first by holding fixed the boundaries obtained in section 3.4 with parameters in Figure 3. Using those to separate the regions of the emission model, equation (4), we fit for the five parameters of that model, A_1, B, α, β, and A_2. We use as initial guess the parameters which were obtained by Jorgensen et al. (2019), $A_1 = 3.2285 \times 10^{-5}$, $B = -1.79847 \times 10^{-5}$, $\alpha = 2.4908$, $\beta = -1.64578$, and $A_2 = 1.35885 \times 10^{-5}$.

Figure 4 shows those parameters as a function of time, which is referenced to orbital position via Figure 2. Figure 4a is for the June 2022 orbit, and Figure 4b is for the April 2022 orbit. In each panel, the solid black curve is A_1, the solid red curve is B, and the solid blue curve is A_2, all referenced to the axis on the left; the dashed red curves is α, and the dashed blue curve is β, both referenced to the axis on the right. For both orbits, we see that in the central time interval, about 12.75 to 14.2 days for the June 2022 orbit and about 11.7 to 13.15 days for the April 2022 orbit, the parameters show much less variation than they do near the ends of the intervals.

In the June 2022 orbit, 12.75 days corresponds to $Z = 14\ R_E$ and the other coordinates small; 14.2 days corresponds to $Z = 8\ R_E$ and $X = 9\ R_E$. In the April 2022 orbit, 11.7 days corresponds to $Z = 13\ R_E$ and the other two coordinates small, and 13.15 days corresponds to $Z = 11\ R_E$ and the other two coordinates smaller though not much smaller. Recollect that at this point, we are fitting to the 3-D emissions distribution. A satellite which is further away will cover a large region of those emissions. It appears that when the volume

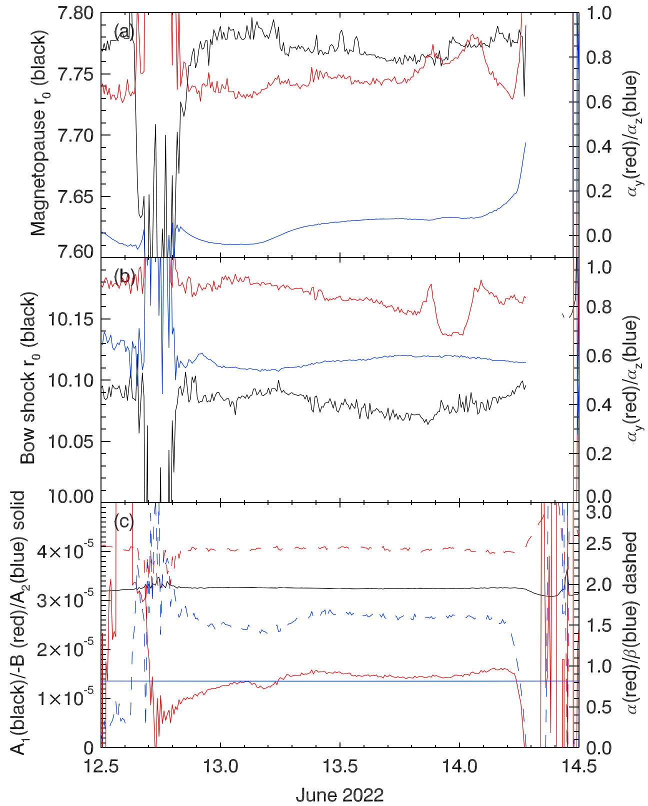

Figure 5. Fits of all 11 parameters to the 3-D emissions distribution model as a function of orbital viewing geometry of Solar Wind Magnetosphere Ionosphere Link Explorer SXI in the June 2022 orbit. The initial guess for the fits are the parameters for the boundary models which were previously fit in Figure 3 and the parameters for the emissions model which were previously fit in Figure 4. (a) plots the boundary model parameters for the magnetopause. The black curve is r_0, referenced to the left-side axis; the red curve α_y and the blue curve α_z, both referenced to the right-side axis. (b) plots the same parameters for the bow shock with the same color scheme as in (a). (c) plots the emissions model parameters in equation (4). A_1 (solid black), $-B$ (solid red), and A_2 (solid blue) are referenced to the left-side axis. α (dashed red) and β (dashed blue) are referenced to the right-side axis.

included in the fit is large, the fit is well-constrained, whereas when it is small or covers only a portion of the dayside magnetosheath and boundaries, the fit is not well-constrained.

3.6. Fitting the Complete Model as a Function of Orbital Viewing Geometry

This is the final step in obtaining what we consider to be best-fit or near-best-fit parameters of the combined model of emissions and two boundaries to the 3-D emissions distribution according to the mean-absolute-deviation cost function. Here we fit for all 11 parameters, r_0^{mp}, α_y^{mp}, α_z^{mp}, r_0^{bs}, α_y^{bs}, α_z^{bs}, A_1, B, α, β, and A_2, of the full 3-D model. The initial guesses for the parameters will be those fit in Figure 3 for the boundary model parameters, r_0^{mp}, α_y^{mp}, α_z^{mp}, r_0^{bs}, α_y^{bs}, and α_z^{bs}, and those fit in Figure 4 for the emissions model parameters, A_1, B, α, β, and A_2. The results of this fitting are shown in Figure 5 for the June 2022 orbit and in Figure 6 for the April 2022 orbit.

What we immediately notice about Figures 5 and 6 is that the curves of fitted parameters are not as smooth as those of previous figures, for example, Figures 3 and 4, but exhibit what we might described as noise. We believe this noise is related to the downhill simplex fitting algorithm finding false minima which are near the optimum fits for the boundary model parameters and brightness model parameters separately.

As with the previous fits, there are times/orbital positions where the fitted parameters show excursions, and those are nearly the same times as in the previous fits, 12.6 to 12.9 for the June 2022 orbit and 11.6 to 12.0 for the April 2022 orbit. For both orbits, there is also a time interval at the end of the descending portion of the orbit where the fit shows excursions, that is, after 14.2 for the June 2022 orbit and after 13.1 for the April 2022 orbit. In the interval of 12.9 to 14.2 for the June 2022 orbit as well as 12.0 to 13.1 for the April 2022 orbit, the fitted parameters are approximately constant. They are also similar to those previously fit

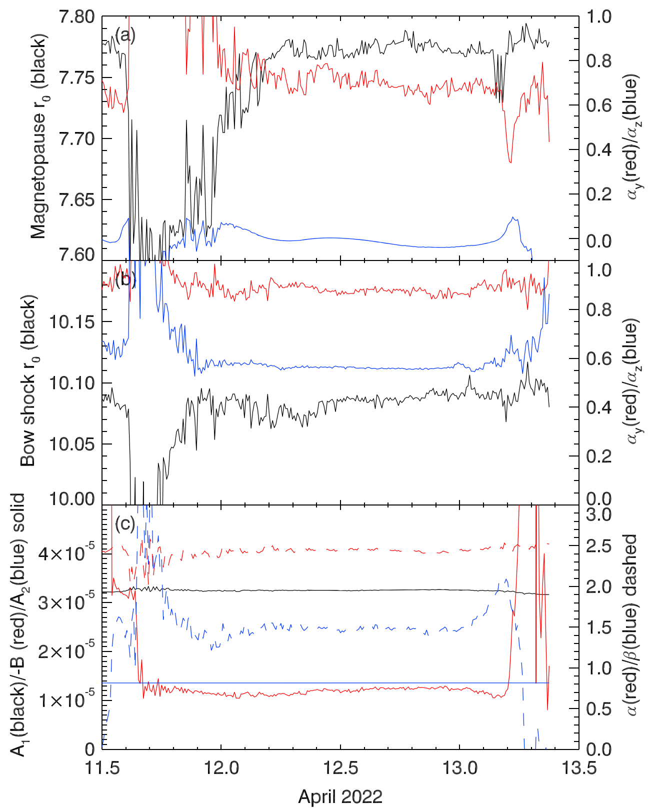

Figure 6. Fits of all 11 parameters to the 3-D emission distribution as a function of orbital viewing geometry of Solar Wind Magnetosphere Ionosphere Link Explorer SXI in the April 2022 orbit. The figure layout is identical to that of Figure 5.

separately for the boundaries and the emissions although there are some differences. Table 1 summarizes average values obtained by visual inspection of the plots. Most parameters agree well between the separate fit and the combined fit, as well as between the June 2022 orbit and the April 2022 orbit. However, two parameters, r_0^{mp} and r_0^{bs}, are smaller by about 0.1 R_E in the combined fit compared to the separate fit. This difference is within the accuracy requirement of the SMILE mission. The likely source of the difference is the difference in the way the boundaries are defined in each case. When fitting the boundary points directly, we use boundary points which are determined from plasma flow analysis. When fitting the combined model, the boundary is defined by X-ray emissions. It is not inconceivable that the two definitions could result in boundaries located at slightly different locations and still comparable to the grid size in the MHD simulation.

We have examined the time periods with bad fits, before 12.9 and after 14.1 for the June 2022 orbit and before 12.0 and after 13.1 for the April 2022 orbit. The fits which do not produce good parameters are ones in which the SMILE SXI FOV does not cover a significant portion of the dayside magnetopause/magnetosheath/bow shock. When only a small region is in the FOV, the fitted parameters can be far away from the nominal parameters. During the times when the SMILE SXI views a larger region, the parameters are much closer to the nominal parameters and are nearly independent of viewing geometry.

3.7. Fitting the Images as a Function of Orbital Viewing Geometry

In the above sections, we followed a careful process which, we believe, resulted in the best fit of the combined 11-parameter model to the 3-D MHD data which is contained in the FOV of the SMILE SXI camera. We found that for the portions of the orbit where the camera has a wide view of the dayside magnetopause, magnetosheath, and bow shock, the parameters fit to the 3-D MHD data are not very sensitive to the orbital viewing geometry. We also found that the fitted parameters of the combined 11-parameter model are similar to the parameters of the boundary models fit to the magnetopause grid points and the bow shock grid points, with some notable offsets; in the combined fit, the location of the subsolar point on the magnetopause is approximately 0.1 R_E closer to the Earth than when fitting to the boundary points.

Table 1
Summary of Average Values of Fitted Parameters Obtained by Visual Inspection of the Plots

	June 2022		April 2022	
Parameter	Separate	Combined	Separate	Combined
r_0^{mp}	7.9	7.78	7.9	7.78
α_y^{mp}	0.7	0.75	0.7	0.7
α_z^{mp}	0.05	0.1	0.0	0.0
r_0^{bs}	10.15	10.08	10.17	10.08
α_y^{bs}	0.8	0.85	0.9	0.9
α_z^{bs}	0.6	0.6	0.6	0.55
A_1	3.2×10^{-5}	3.2×10^{-5}	3.2×10^{-5}	3.2×10^{-5}
B	-1.5×10^{-5}	-1.2×10^{-5}	-1.2×10^{-5}	-1.1×10^{-5}
α	2.5	2.5	2.5	2.4
β	1.6	1.5	1.5	1.4
A_2	1.3×10^{-5}	1.3×10^{-5}	1.3×10^{-5}	1.3×10^{-5}

Note. The first column contains the parameter name, the second the value obtained for the June 2022 orbit by separate fitting of boundary and emissions, the third the value obtained by combined fitting. The fourth and fifth columns correspond to the second and third but for the April 2022 orbit.

Now that we have, after some effort, obtained the best-fit, or near-best-fit, parameters for the full model to the 3-D emissions, it is time to fit the images and determine how well the parameters from the 2-D image fits compare with the results of the best-fit model. At each point in the orbit, we simulate images from the X-ray emissions derived from the 3-D MHD model. The procedure for doing this is thoroughly described by Jorgensen et al. (2019) in their section 2.3. We then fit for the parameters of the analytical model by minimizing the difference between the image generated from the 3-D emissions from the MHD model and the image generated from the analytical model, equation (4), using equation (1) for each of the two boundaries. It is similar to the combined model fit in the previous section except that we compare the images instead of the 3-D emissions distribution. The cost function is still the mean-absolute difference, this time the mean-absolute difference of pixel values. For this fit, we find that the initial guess is particularly important for the minimum point reached. By using best-fit parameters from Figures 5 and 6, we have some confidence that the minimum arrived at is the global minimum, but we will test that in one example later.

Figures 7 and 8 show the results for the June 2022 and April 2022 orbits, respectively. The most interesting parameters are those for the boundaries so in the interest of brevity we show only those. Figures 7a and 8a are for the magnetopause, and Figures 7b and 8b are for the bow shock. In each panel, the dashed curves represent the initial guesses for the fit, taken from Figures 5 and 6. The black curves are for r_0, referenced to the left-hand axis; the red curves are for α_y and the blue curves for α_z, both referenced to the right-hand axis.

To a certain extent, the solid curves (the fit to the 2-D images) agree with the dashed curves (the carefully arrived at best-fit to the 3-D emissions distribution). We note that differences between the two sets of curves appear larger at the beginning of the intervals, before about 12.85 days in the June 2022 orbit and before about 11.85 days in the April 2022 orbit. These intervals have particularly poor image coverage of the emissions distribution, so we do not expect a good fit.

First, we examine the magnetopause parameters for the June 2022 orbit, in Figure 7a. α_y obtained from the images (red solid) is in very close agreement with the value obtained from the 3-D emissions distribution, except at the ends of the orbit. α_z is also in good agreement between image and 3-D emissions distribution although the value derived from the images is biased a little higher, perhaps 0.05 to 0.1. For the magnetopause position, r_0, the trend is very similar although there is an offset between the values with the image-derived value larger, perhaps by 0.15 R_E. Notice that this puts the image-derived value for r_0 in better agreement with the value derived from fitting directly to the boundary points. We believe this change is again a function of the changing definition of the boundary between the boundary detection, the X-ray emissions in the 3-D distribution, and the boundary in the images.

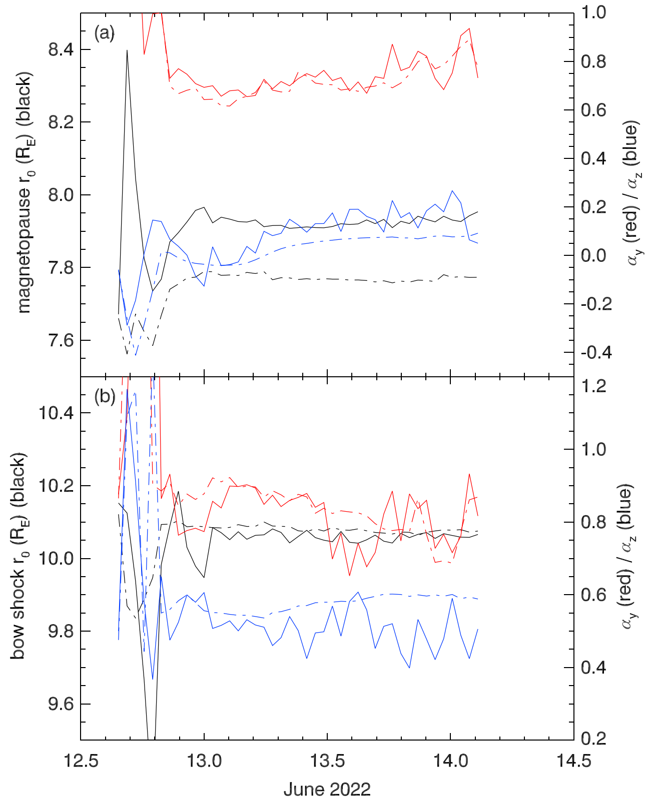

Figure 7. Fit of all 11 parameters to 2-D images, using the previous fits, from Figure 5 as initial guess, for the June 2022 orbit.

Next let us look at the magnetopause for the April 2022 orbit, in Figure 8a. We see a very similar result to the June 2022 event with some notable differences. α_y is in good agreement between the fit to the 3-D emissions and the fit to the 2-D images. α_z shows only a small bias and for the April 2022 orbit toward smaller values. α_z also shows several negative outliers, for example, near 11.8, 11.9, 12.0, and 12.4, and each of those are accompanied by a positive outlier in r_0. Aside from these outliers, r_0 behaves in a very similar way to the June 2022 event in terms of the positive offset of about 0.15 which puts it in better agreement with the value derived directly from fitting the boundary points.

For the bow shock, r_0 is in good agreement for both the April 2022 and the June 2022 orbits (black curves in Figures 7b and 8b) although there are several positive outliers in r_0 for the April 2022 orbit. For the case of α_y for June 2022, the value obtained from the fits to the 2-D images is mostly in good agreement with the values from the fits to the 3-D emissions, even as the values from the fits to the 3-D emissions show some variation with time. For the April 2022 orbit, the situation is different; there appears to be an offset of size 0.1 for the majority of the orbit, with the value for the image fit being smaller than the value for the 3-D distribution fit. For α_z, there are also differences between the two orbits. For the April 2022 orbit, the values from the image fits are mostly close to the values from the fits to the 3-D distribution, except for several negative outliers which correspond with the positive outliers in r_0. They also correspond with the outliers in the magnetopause parameters.

4. Discussion

Reviewing the results from section 3.7, we find that for the most part, the agreement is good between parameters obtained from the 2-D images fits and parameters obtained from the 3-D emissions fits. The differences between the two are comparable to the size of the grid in the 3-D MHD model. There are systematic differences in the location of the magnetopause between fits to the 3-D emissions and fits to the 2-D images which are similar to the size of the 3-D MHD model grid. We can speculate that the differences can be related to differences in how the boundaries are defined. The boundary is defined in terms of flux for the gridded

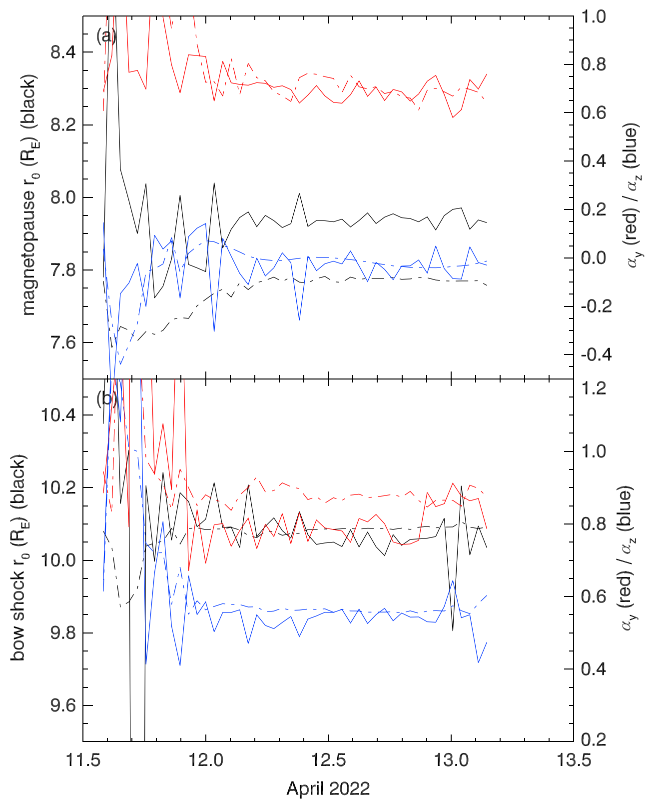

Figure 8. Fit of all 11 parameters to 2-D images, using the previous fits, from Figure 6 as initial guess, for the April 2022 orbit.

boundary points, and the emissions are set to zero inside of the magnetopause boundary. However, we also know that this boundary does not exactly match the boundary seen in the emissions and that there can be a difference of one or two grid cells between where the emissions drop and where the boundary is detected by the flux method. This can be seen in some of the figures presented by Jorgensen et al. (2019). The result can be a shift of the boundary by a small amount, of the order of the grid spacing.

Despite the few outliers, we find that for the most part, the parameters which are the best fit to the 3-D distribution appears to also be the best fit to the 2-D image and not vary much with orbital viewing geometry. This is exactly what we hoped for.

In consideration of the few outliers, it is worth exploring the cost-function landscape for false minima in the vicinity of the best-fit parameters from Figures 5 and 6. It is not straightforward to map out the cost-function landscape to any level of detail, even for a single image or satellite position. If we want simply 10 evaluations along each dimension of the cost-function landscape, we must evaluate the cost function some 10^{11} times. By comparison, a simplex downhill climb fit typically requires a few thousand evaluations of the cost function for this problem before it finds a minimum.

Instead of mapping out the search space, we attempt to get an overview of it by carrying out many fits from different initial guesses for a single image, corresponding to day 12.14 in the April 2022 orbit. We chose 100 guesses by selecting an independent Gaussian randomly distributed value for each of the 11 parameters. They are as follows: the mean value plus or minus the standard deviation, $A_1 = 3.2\times10^{-5} \pm 0.5\times10^{-5}$, $B = -1.8\times10^{-5} \pm 0.5\times10^{-5}$, $\alpha = 2.5 \pm 1$, $\beta = -1.6 \pm 0.5$, $A_2 = 1.35\times10^{-5} \pm 0.5\times10^{-5}$, $r_0^{\mathrm{mp}} = 8 \pm 1$, $\alpha_y^{\mathrm{mp}} = 0.7 \pm 0.3$, $\alpha_z^{\mathrm{mp}} = 0.1 \pm 0.3$, $r_0^{\mathrm{bs}} = 10 \pm 1$, $\alpha_y^{\mathrm{bs}} = 0.8 \pm 0.3$, and $\alpha_z^{\mathrm{bs}} = 0.6 \pm 0.3$.

We present the results in two different ways. To visualize the 11-dimensional space of parameters, we show several projections onto two-dimensional planes in Figure 9. In each panel, the two axes are two of the parameters. The panels contain straight lines between the final fitted value (the end of the line with a dot) and the initial guess (the end of the line without a dot). The color of the line and dot is a function of the

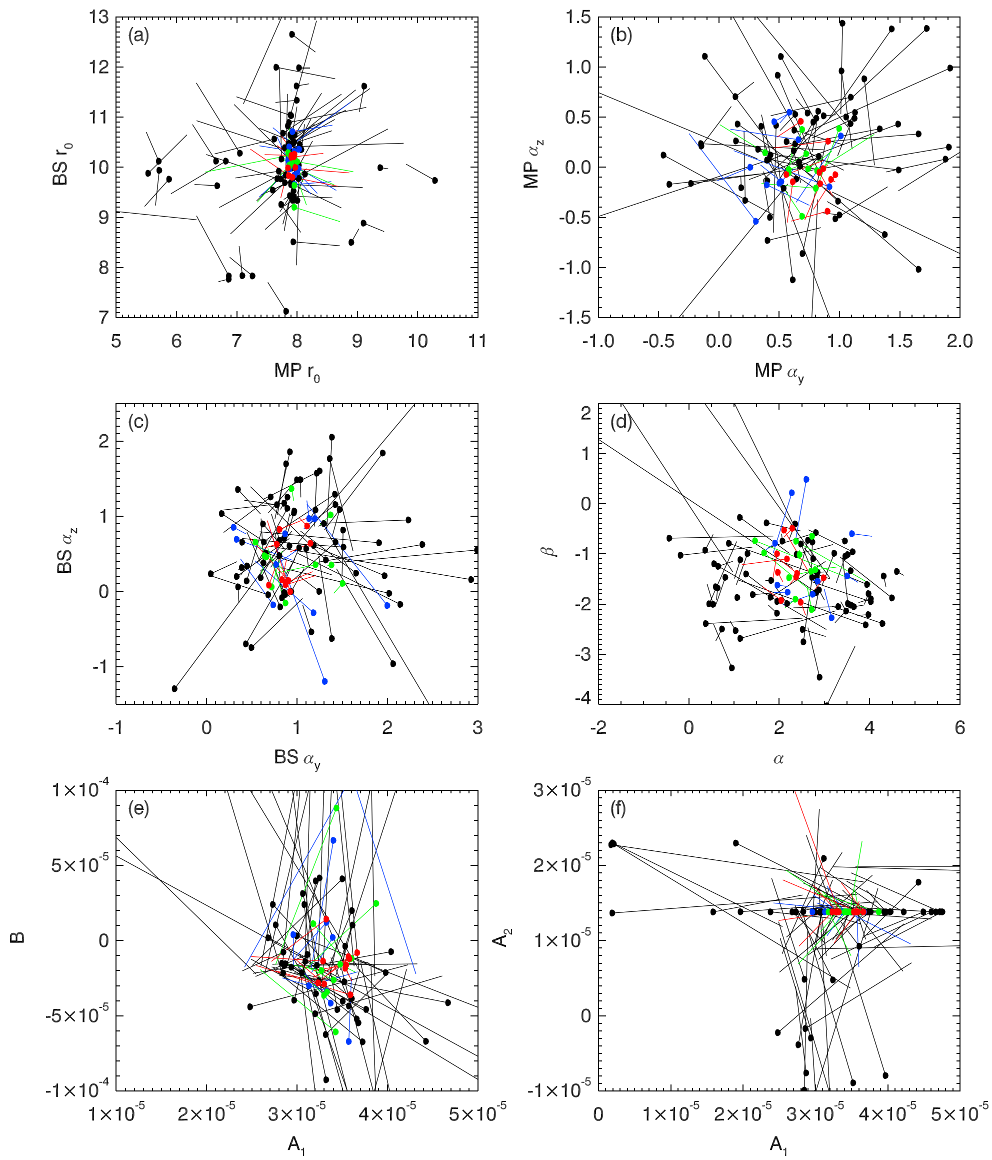

Figure 9. Each panel is a projection onto a plane as follows: onto the (a) r_0^{BS} versus r_0^{MP} plane, (b) α_z^{MP} versus α_y^{MP} plane, (c) α_z^{BS} versus α_y^{BS} plane, (d) β vs α plane, (e) B versus A_1 plane, (f) A_2 vs A_1 plane. This suggests that there are many false minima.

depth of the minimum. The red dots are the 10% deepest minima, the green the next 10% deepest minima, blue the next 10% deepest, and black the remaining, the 70% shallowest minima.

In Figure 9a, we see a narrow distribution of the 10% deepest minima in r_0^{mp} and a somewhat less narrow distribution of those points in r_0^{bs}. In Figure 9f, we can see that most points fall close to the best-fit value for A_2 and the points with the deepest minima are also close to the best-fit value for A_1. It is perhaps not surprising that A_2 is easier to fit as the emission sunward exactly follows the functional form of equation (4) with parameter A_2 and does not mix with other parameters in that region. The only possibility for getting the wrong value for A_2 is if the bow shock is in the wrong location forcing a fit to values which do not follow the function.

In Figure 10, we plot the normalized depth of the minimum as a function of the normalized distance from the best-fit minimum. The normalized depth of minimum is the minimum cost-function value divided by the best-fit minimum. The normalized distance from the best-fit minimum is found by taking the normalized distance along each axis and adding those in quadrature, taking the square root, and dividing by $\sqrt{11}$. The

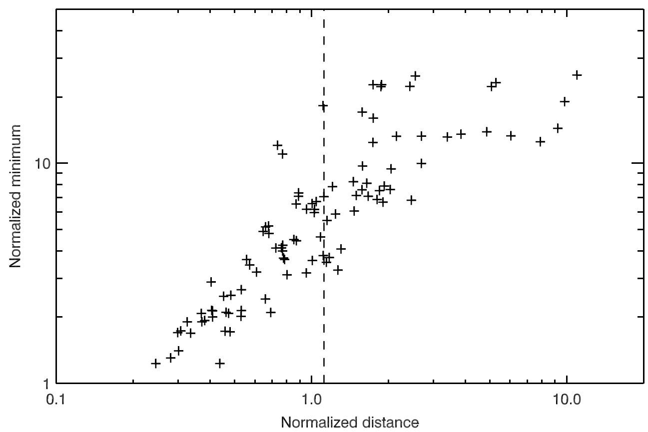

Figure 10. Plot of normalized depth of minimum versus normalized distance from presumed optimal fit. This plot suggests that the procedure we used to find initial guesses works well and that there is a well-defined global minimum.

normalized distance along one axis is the distance from the best-fit value along that axis divided by the standard deviation along that axis. With this distance measure, we expect the average and median distance of points to be approximately one. If the best-fit minimum is indeed the best-fit, we expect all normalized minima to be greater than one. We also find that to be true. We also find an increasing minimum value with increasing distance from the best-fit minimum. We conclude that we have in all likelihood found the best fit through our procedure.

Because the cost-function landscape is complicated, it is worth looking for simplifications. One to consider is based on the soft degeneracy between α_z and r_0. α_z and α_y determine the curvature of the boundaries, but because SMILE SXI views only a small section of each boundary near the subsolar point and as such choosing nominal values for each, based on measured solar wind conditions, may simplify the fitting problem. This and the design of the fitting algorithm are things which should be considered as these results move toward operational tools to be used for data analysis during the SMILE mission.

5. Conclusion

We have worked through a careful analysis to determine the best-fit parameters for the model previously presented by Jorgensen et al. (2019) to 3-D X-ray emissions distribution derived from a MHD model. We fit the model to the 3-D emissions point which fall within the FOV of the SMILE SXI camera for different orbital viewing geometries. We found that the fitted model parameters do not vary much with the viewing geometry except when the FOV misses essential elements such as the subsolar point of the magnetopause and bow shock.

We then used these fits as the initial guess in fitting the same model to 2-D images of the X-ray emissions. We found that for the most part, the fits to the 2-D images are able to determine the model parameters and that those agree well with previous fitted parameters and do not show orbital bias.

We also carried out an experiment with one orbital viewing geometry to look at the prevalence of false minima and whether it is possible to find deeper minima than the ones we determine by the process we developed. We found that there are many local minima but that none were as deep as that determined by the process.

We believe the likelihood of fitting a false minimum can be reduced by using a better fitting algorithm than the simplex method we used or by reducing the dimensionality of the problem, for example, by fixing α_z and α_y.

Acknowledgments
This work was supported by NNSFC grants 41731070, 41774173, and 41574159; Key Research Program of Frontier Sciences, CAS, grant QYZDJ-SSW-JSC028; and Strategic Pionner Program on Space Science, CAS, grant XDA15052500 and XDA 15350201. The author Tianran Sun was also supported by the Young Elite Scientists Sponsorship Program by CAST (2017QNRC001) and the Youth Innovation Promotion Association (2016134). Files containing the X-ray volume emission and magnetopause boundary location used as the input to all the simulations, as well as IDL-language code to read those files, may be downloaded online from the Open Science Framework (osf.io/r5jbg; Jorgensen et al., 2019).

References

Carter, J., Sembay, S., & Read, A. (2010). A high charge state coronal mass ejection seen through Solar Wind Charge Exchange emission as detected by XMM–Newton. *Monthly Notices of the Royal Astronomical Society*, *402*(2), 867–878.

Cravens, T. (1997). Comet Hyakutake X-ray source: Charge transfer of solar wind heavy ions. *Geophysical Research Letters*, *24*(1), 105–108.

Jorgensen, A. M., Sun, T., Wang, C., Dai, L., Sembay, S., Wei, F., et al. (2019). Boundary detection in three dimensions with application to the the smile mission: The effect of photon noise. *Journal of Geophysical Research: Space Physics*, https://doi.org/10.1029/2018JA025919

Kronrod, A. S. (1965). *Nodes and weights of quadrature formulas*. New York: Consultants Bureau.

Lin, R., Zhang, X., Liu, S., Wang, Y., & Gong, J. (2010). A three-dimensional asymmetric magnetopause model. *Journal of Geophysical Research*, *115*, A04207. https://doi.org/10.1029/2009JA014235

Lisse, C., Dennerl, K., Englhauser, J., Harden, M., Marshall, F., Mumma, M., et al. (1996). Discovery of X-ray and extreme ultraviolet emission from Comet C/Hyakutake 1996 B2. *Science*, *274*(5285), 205–209.

Nelder, J. A., & Mead, R. (1965). A simplex method for function minimization. *The Computer Journal*, *7*(4), 308–313.

Raab, W., Branduardi-Raymont, G., Wang, C., Dai, L., Donovan, E., Enno, G., et al. (2016). Smile: A joint ESA/CAS mission to investigate the interaction between the solar wind and Earth's magnetosphere. In *Space telescopes and instrumentation 2016: Ultraviolet to gamma ray* (Vol. 9905, pp. 990502). Edinburgh, UK: International Society for Optics and Photonics.

Shue, J.-H., Chao, J., Fu, H., Russell, C., Song, P., Khurana, K., & Singer, H. (1997). A new functional form to study the solar wind control of the magnetopause size and shape. *Journal of Geophysical Research*, *102*(A5), 9497–9511.

Sibeck, D. G., Allen, R., Aryan, H., Bodewits, D., Brandt, P., Branduardi-Raymont, G., et al. (2018). Imaging plasma density structures in the soft X-rays generated by Solar Wind Charge Exchange with neutrals. *Space Science Reviews*, *214*(4), 79.

Snowden, S., Collier, M., Cravens, T., Kuntz, K., Lepri, S., Robertson, I., & Tomas, L. (2009). Observation of Solar Wind Charge Exchange emission from exospheric material in and outside Earth's magnetosheath 2008 September 25. *The Astrophysical Journal*, *691*(1), 372.

Sun, T. R., Wang, C., Sembay, S., Lopez, R. E., Escoubet, P., Branduardi-Raymont, G., et al. (2019). Soft X-ray imaging of the magnetosheath and cusps under different solar wind conditions: MHD simulations. *Journal of Geophysical Research: Space Physics*, *124*. https://doi.org/10.1029/2018JA026093

Wolpert, D. H., & Macready, W. G. (1997). No free lunch theorems for optimization. *IEEE Transactions on Evolutionary Computation*, *1*(1), 67–82.